



Microstructural Nano-Scale Evolution at Inter-Particles Bonding Interface of Cold-Sprayed Ti6Al4V Deposits During Heat Treatment

Lijing Yang^{1,3} · Shaopeng Wang^{1,3} · Xiaotao Luo² · Pei Wang^{1,3} · Haiyu Yang^{1,3} · Huan Li^{1,3} · Jiayi Xiang^{1,3} · Xue Bai^{1,3}

Submitted: 2 August 2023 / in revised form: 21 September 2023 / Accepted: 23 September 2023 / Published online: 11 October 2023
© ASM International 2023

Abstract The inter-particle bonding (IPB) mechanism of cold-sprayed titanium alloy during heat treatment (HT) is not clear. The interfacial microstructure and bonding characteristics at the interface of cold-sprayed Ti6Al4V after HT were studied at the micro- and nano-scale. As a result, the nanocrystallization at IPB during cold spray (CS) cannot cause obvious metallurgical bonding between Ti6Al4V particles. The average Young's modulus of CS Ti6Al4V is 57% higher than that of powder, but the average Young's modulus of HT sample decreases by 16%. The internal stress and dislocation distribution of interfacial microstructure can lead to various microstructure features and non-uniform rates of microstructure growth at deformed transition layer and IPB during HT. The nanograins at the IPB grow into micron-equiaxed grains. On the contrary, the micron martensitic laths at deformed transition layer adjacent to IPB show the characteristics of equiaxed nanograins transformation under the action of grain boundary bulges induced by dislocation entanglement.

Keywords additive manufacturing · bonding mechanism · cold spray · heat treatment · interface · titanium alloy

Introduction

Cold spray (CS) has shown potentials in additive manufacturing industries and attracted worldwide interests due to the important benefits of high deposition efficiency, unlimited product size and high flexibility (Ref 1, 2). As a new member of the additive manufacturing family, cold-sprayed deposits generally have unfavorable mechanical properties in their as-fabricated state compared to conventionally manufactured and fusion-based additive-manufactured counterparts. This phenomenon is resulted from the inherent microstructural defects in the cold-sprayed deposits (e.g., porosity, interfacial impurity, and incomplete inter-particle bonding) (Ref 3-5). Titomic Limited presented a model of a titanium alloy rocket using cold spray additive manufacturing at FORMNEXT exhibition in 2019. Titanium alloys as lightweight structural material have been widely used in aerospace, shipbuilding, nuclear industries because of its high strength-to-weight ratio and excellent seawater corrosion resistance (Ref 1, 6, 7). However, the titanium alloys with high hardness are difficult to deform in CS process, which can easily result in the high porosity and weak inter-particle bonding (IPB) of the titanium deposits. The porosity and weak IPB have been widely recognized as the main factor of poor mechanical properties of cold-sprayed titanium alloy. In recent years, the unique, coral-like morphology design of the CP-Ti and Ti6Al4V powders is an effective way to improve the density of deposits; CP-Ti deposits sprayed with nitrogen result in a grain size of $1 \pm 0.6 \mu\text{m}$, while deposits processed with helium result in a grain size of $0.7 \pm 0.2 \mu\text{m}$ with no clear difference between the grain size at particle interiors and at prior particles boundaries (Ref 8). Birt A. had demonstrated that the mechanical deformation of martensitic Ti6Al4V powder in CS could not only create a

✉ Lijing Yang
yanglj@c-nin.com

¹ Northwest Institute for Non-ferrous Metal Research, Xi'an 710016, Shaanxi, China

² State Key Laboratory for Mechanical Behavior of Materials, School of Materials Science Engineering, Xi'an Jiaotong University, Xi'an 710049, Shaanxi, China

³ Rare Metal Materials Surface Engineering Technology Research Center of Shaanxi Province, Xi'an 710016, China

nanostructured material, but also be used to adjust the level of transformation in the microstructure (Ref 9). In addition, the CS composite technology is also an effective way to improve the density of titanium alloy CS deposits, such as in situ shot peening, laser assisted, friction stir processing, hot-rolling, and high current pulsed electron beam irradiation (Ref 10–17). Nevertheless, the IPBs in the CS deposits are mainly mechanical bonding (Ref 18, 19). The intrinsic IPBs in the CS deposits are the defects source of failure in the evaluation of mechanical properties (Ref 2, 20).

In order to enhance atomic diffusion of the interface bonding and release the internal stress, the heat treatment (HT) is considered to be the most effective means to improve mechanical properties of CS deposits (Ref 21). Huang R. reported that all the mechanical properties of CS samples improved with the increasing of HT temperature; the tensile strength and elongation of CSed Ti coatings were less than 200 MPa and 0.5%, which was extremely low compared with that of the bulk Ti (even when heat-treated at a higher temperature of 1000 °C). After HT at 400 ~ 500 °C, the tensile strength and elongation of CSed Cu coating even exceeded that of the bulk Cu (Ref 22). Li W. et al. found that many interfaces between the deposited Ti particles disappeared by means of annealing at 850 °C for 4 h under vacuum, and the adhesive strength of the Ti deposits was significantly improved from 19 MPa to over 50 MPa after annealing (Ref 23). Vo P. reported that the nitrogen-sprayed Ti6Al4V coatings annealing at 1000 °C could only produce an improvement to ~ 50% of the bulk strength as well as a phase transformation. However, the near-dense coatings produced with helium annealing at 600 °C produced a tensile strength ~ 85% of the minimum required bulk value, while maintaining the as-received microstructures of the powder and substrate (Ref 24). It was known that CS Ti6Al4V deposition showed difficulties to obtain non-porous coatings due to the high strength of titanium alloys. The mechanical properties of lower porosity CS Ti6Al4V coatings sprayed at a process gas temperature of 1100 °C and a pressure of 50 bar were improved by a post-heat treatment performed with a 1000 °C. The cohesive strength of the HTed coating was ~ 1200 MPa, and it was significantly higher than that of the as-sprayed coating, ~ 350 MPa (Ref 25).

The microstructural features and evolutions at IPB for cold-sprayed Ti6Al4V with a post-heat treatment have not been discussed in detail. In order to explore the intrinsic reason of poor mechanical properties of the CS deposits, the basic researches on the bonding mechanism of IPB were carried out at the micro- and nano-scale. Chen et al. (Ref 26) had proved the cleaning effect produced by the extrusion of viscous metal jet by the observation of oxides fragments located at the periphery of detached particle,

which promoted the formation of metallurgical bonding around central area. Ichikawa et al. (Ref 27) revealed that the “south-pole problem” of CS particles could lead to decrease in the overall adhesion strength despite the local adhesion being strong by auger electron spectroscopic evaluation of bonding interface oxide film. The dislocation density in cold-sprayed Al-Cu binary alloys with intentionally varied composition was quantified using CMWP analysis of the x-ray diffraction profiles (Ref 28). The heterogeneous microstructural evolution in cold-sprayed copper coatings was predicted using local Zener-Hollomon parameter and strain (Ref 29). However, the effectiveness of HTed feedstock powder to improve the mechanical properties of CS deposits had also been explored. The ultimate tensile strength of the deposits made with preheated Fe powder approximately doubles to non-preheated powder due to the enhanced intersplat bonding (Ref 30). The ductility of Cu coatings prepared by CS significantly was improved by the recrystallization of coating after HT (Ref 22, 31). Author’s previous research has reported that the coarse martensitic laths of Ti6Al4V particles at the interface were transformed into nanograins by dynamic recrystallization in the process of high speed particle impact (Ref 19). In a word, most of studies have mainly focused on the interfacial bonding mechanism of the CS deposits, but the evolution behavior of interfacial microstructure during HT is less concerned. Therefore, the structural evolution behavior of CS Ti6Al4V deposits at the IPB after HT is characterized and discussed in this paper.

Experimental Details

Materials

Commercial Ti6Al4V powder (6.32 wt.% Al, 4.24 wt.% V, 0.205 wt.% Fe, 0.086 wt.% O, < 0.018 wt.% C N H, bal. Ti) prepared by plasma rotating electrode process atomization (Xi’an Ouzhong Material Technology Co., Ltd, China) was used as the spraying powders. Volumetric size distributions of the Ti6Al4V powder were measured by a laser particle size analyzer (Horiba LA-920, Japan). Sizes of the Ti6Al4V particles range from 10 to 50 μm with an average value of 28.9 μm. As illustrated in Fig. 1(a) and (b), the Ti6Al4V feedstock particles are mainly comprised of the martensitic laths. The martensitic microstructure is characterized by a long, directionally branched laths structure due to the rapid solidification of molten Ti6Al4V droplets during the plasma atomization process (Ref 32). The EBSD images of Ti6Al4V powder are shown in Fig. 1(c) and d. As the band contrast (BC) of Ti6Al4V powder shown in Fig. 1(c), the darker area

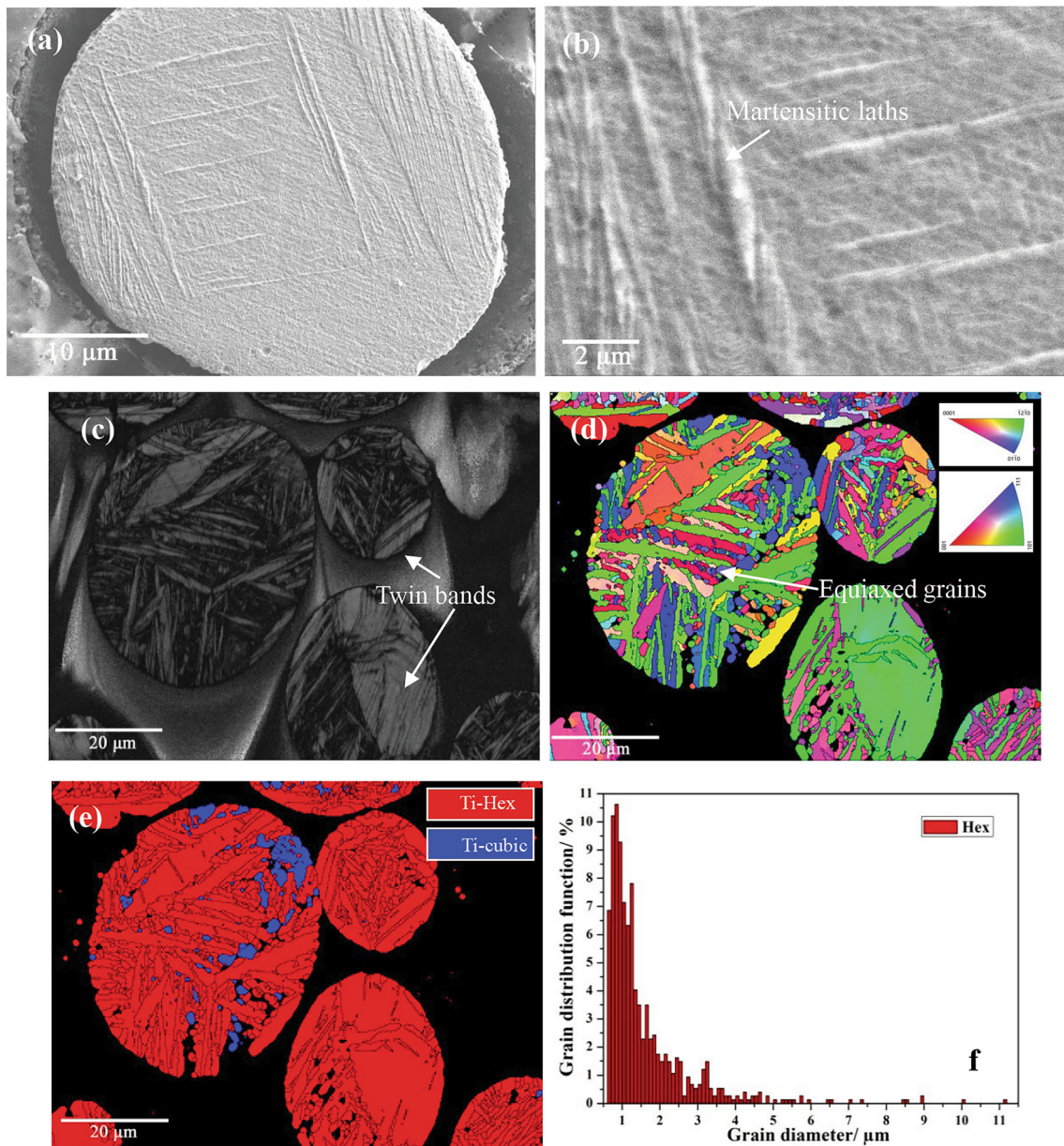


Fig. 1 SEM and EBSD images of the cross-sectional microstructure of Ti6Al4V powder: (a) SEM of single particle, (b) magnification of (a), (c) BC of particles, (d) IPF map of particles, (e) phase distribution, (f) grain distribution of Hex phase

between the brighter martensitic laths indicates that there are dislocation or strain defects at the IPB. Moreover, the twin bands can additionally be observed in the brighter martensitic zone, which is a common feature in hexagonal close packed (HCP) metals. Inverse pole figure (IPF) of Ti6Al4V powder as presented in Fig. 1(d), the orientations of the martensitic laths are random. On the contrary, the twin bands present preferred orientation, and the microstructure between martensitic laths is equiaxed grains. Fig. 1(e) shows that the hexagonal (Hex) phases and cubic phases in the Ti6Al4V particles are 97.58% and 2.42%, respectively. The grain distribution of Hex phase in

the Ti6Al4V particles is shown in Fig. 1(f). The surface of substrates was prepared by blasting using 60 Mesh Al_2O_3 ; then, ultrasonic cleaning in alcohol bath was used to remove the residual sand grits on the substrate surface.

Coating Deposition

The Ti6Al4V coatings were deposited on the commercial Ti6Al4V substrates (Western Superconducting Material Technology Co., Ltd, Xi'an, China) with dimensions of $100 \times 100 \times 8$ mm using a commercially PCS-1000 cold spray system (Plasma Giken Co., Ltd, Japan) with N_2 as the

working gas. In this cold spray system, the spray Ti6Al4V powders were fed into the nozzle along the axis. A convergent-divergent Laval nozzle made of WC-Co cermet was used with a throat diameter of 2.7 mm, an outlet diameter of 6 mm and a divergent section length of 150 mm. The N₂ gas was used as the accelerating gas and powder carrier gas. The pressure and temperature of the propelling N₂ gas were set as 4 MPa and 800 °C, respectively. The standoff distance between the nozzle exit and the substrate surface was 20 mm. The gun traverse speeds are 40 mm/s. To a certain extent, the quality of coating also improves with the increase in gas temperature and pressure. However, the maximum working pressure and gas temperature of commercial cold spraying equipment are 5 MPa and 1000 °C, respectively. On the one hand, higher gas pressure leads to higher gas consumption and thus cost (e.g. > 1200 L.min⁻¹ when gas pressure is > 5 MPa) (Ref 26). On the other hand, higher gas temperature such as 1000 °C can improve the coating quality, but it will lead to serious oxidation of the Ti6Al4V particles. Considering spraying cost, oxidation defect control and equipment, the gas pressure and temperature of 4 MPa and 800 °C are relatively suitable for industrial application of Ti6Al4V deposition. The α and β phase transition points of the Ti6Al4V alloy are 882 °C. In order to prevent the effect of phase transition from α to β on the microstructure evolution, the coating samples were annealed at 850 °C for 60 min at argon atmosphere.

Microstructure Characterization

A field emission scanning electron microscopy (SEM, SU6600/5000, Japan) with an electron backscatter diffraction (EBSD, Oxford Symmetry, UK) system was carried out to characterize the cross-sectional grain orientation distribution of the CS Ti6Al4V deposits. The sawed samples were firstly mounted into epoxy resin and then ground by SiC abrasive paper after they were solidified and finally polished by a 0.1 μ m diamond polish agent. The samples were then ultrasonically cleaned in an ethanol bath for 10 min to remove the adhered polish agent. Due to the high residual stress of Ti6Al4V particles and deposits, the EBSD samples were ground by 1200 grit abrasive paper to obtain a relatively smooth finish, then which were polished for 6 h using a vibratory polisher (VibroMetTM2, Buehler, USA) with a 0.05 μ m colloidal silica attack polish on a medium-napped chemical pad and were further milled using Argon ion. The spatial and angular resolutions of the EBSD system were 50 nm and 0.5°, respectively. The acceleration voltage used was 20 keV, and the step size was 100 nm. The recorded EBSD data were post analyzed using Oxford Instruments Channel 5 software. Slight etching was performed on the finely polished cross-

sectional microstructures using 1 ml HF: 4 ml HNO₃: 45 ml H₂O solution for 5 s to reveal inter-particle boundaries. The interfacial microstructures between Ti6Al4V particles were also characterized by a transmission electron microscope (TEM, Tecnai G2 F30, FEI, USA) at 200 keV. The focused ion beam (FIB, Helios G4, FEI, USA) was used to cut the TEM sample from the interfacial microstructure area with a sample size of 8 × 10 μ m and a sample thickness of about 1 μ m. Then, the samples were milled to the thickness of 50 nm using ion beam. The sample was characterized by bright field image (BF), dark field image (DF), high-resolution transmission electron microscope (HRTEM), selected area electron diffraction patterns (SADPs) and fast Fourier transform algorithm (FFT). The Young's modulus, nanohardness and load displacement curves Ti6Al4V particles, the CS deposits and the HT deposits are measured using the nanoindentation method with the load of 7 mN. In order to ensure that the nanoindentation can cover the intact deformed Ti6Al4V particles, the indentation interval is 4 μ m.

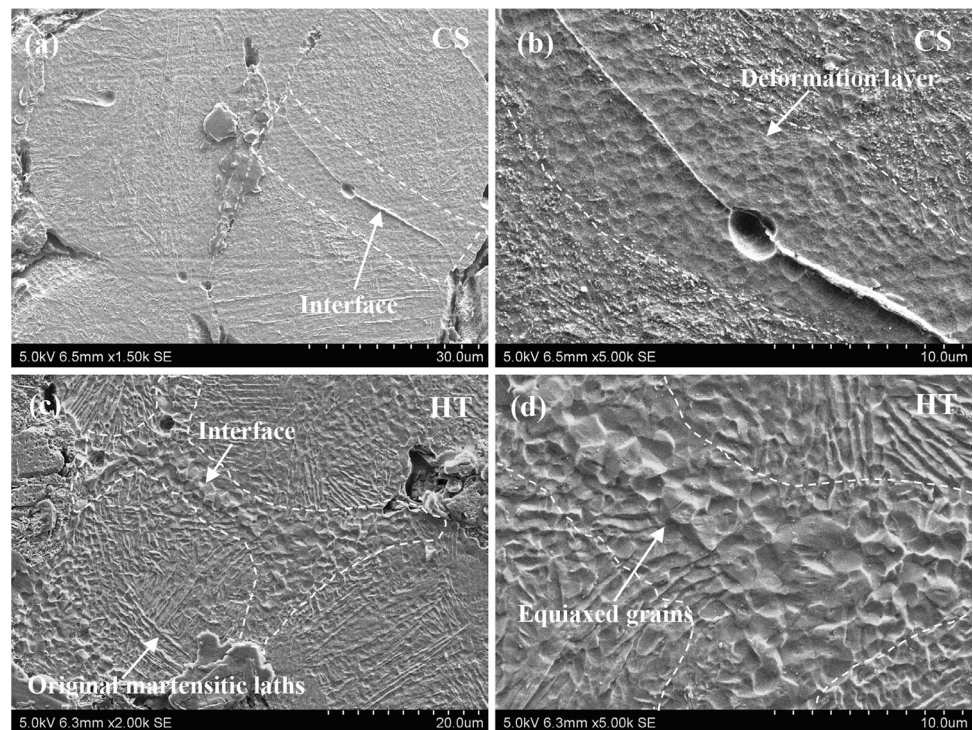
Results and Discussion

Microstructure

To observe the microstructure evolution process at the IPB of heat-treated deposits, the sample was annealed at 850 °C for 60 min at argon atmosphere. The interfacial microstructure of CS deposits before and after HT is shown in Fig. 2. The deformed layer in the Ti6Al4V particle near the bonding interface with a thickness of 5–10 μ m is feature by ultrafine grain which is different from the martensitic laths of the un-deformed zone, as shown in Fig. 2(a) and (b). Previous studies have indicated that the equiaxed nanograins are prone to be formed by dynamic recrystallization at IPB between Ti6Al4V particles (Ref 19). However, the SEM images of CS Ti6Al4V deposits after HT are shown in Fig. 2(c) and (d), the nanograins at the IPB preferentially grow into submicron-scale grains, and the martensitic laths in the deformation layer adjacent to IPB show grain refinement trend.

The EDS mapping and regional element content analysis were used to analyze the white protrusions at the interface between Ti6Al4V particles in the cold-sprayed deposits, as shown in Fig. 3 and Table 1. The oxygen contents of spectrum 1 and 2 were 11.22 and 2.76 wt.%, respectively. The EDS mapping results also showed that there was an obvious accumulation of oxygen elements in the white protrusions at the interface. The EDS results showed that the oxygen content of the white protrusions at the interface was significantly higher than that in other areas of the Ti6Al4V particles, which proved that the white protrusions

Fig. 2 SEM images of cross-sectional microstructure before and after HT at IPB of cold-sprayed Ti6Al4V deposits: (a) CS, (b) CS interface, (c) HT, (d) HT interface



at the interface were titanium oxides. Figure 2(c) and (d) shows that the white oxides and boundary both Ti6Al4V particles after heat treatment disappear. The disappearance of the oxide film can be attributed to the fragmentation and migration of the oxide film under the action of adiabatic shear instability during HT. Under the cold spraying produced much higher strain and strain rate, the micro-sized α -Al₂O₃ on the powder surface crushed into nano-size with discontinuous distribution along the interface between the deformed powders and the plastic flow generated by adiabatic shear made the Al₂O₃ fragments migrated and formed dispersion distribution along the interface (Ref 33, 34). After annealing, the trapped Cu₂O films in the particle-particle interfaces of the as-sprayed Cu coatings break up into particles and coarsen following classical interfacial phenomena including capillary instability, thermal grooving, edge retraction/pinch-off of film, and Ostwald ripening (Ref 31).

EBSD Analysis of Interface

The band contrast (BC), grain orientation and grain size distribution of cross-sectional microstructure of CSed and HTed Ti6Al4V deposits were analyzed using EBSD scanning, as shown in Fig. 4. The BC map and grain orientation of un-annealed CS sample at IPB are shown in Fig. 4(a) and (e), the BC map of the deformation layer of Ti6Al4V particles was darker than that of other areas and the grain orientation map corresponding to the dark region

was also black, indicating that no grain orientation signals had been detected. The brighter areas in the BC map indicate the more perfect the lattice structure. However, on the one hand, the darker area is due to dislocation and residual stress, and on the other hand, the EBSD spatial resolution is insufficient to detect the small size of the nanograins. The martensitic microstructure of Ti6Al4V particles is transformed into nano-equiaxed crystalline structure near the bonding interface during the inter-particles impact. The thickness of the nanocrystalline deformation layer is about 10 μ m and the grain size at the interface with the thickness of 2 μ m is larger than that of the deformation layer. See the grain distribution in Fig. 4(c), it is found that the 63.25% of hexagonal (Hex) grains size are smaller than 1 μ m. The BC map and grain orientation of HT sample at IPB are shown in Fig. 4(b) and (f), the BC map of the deformation layer of Ti6Al4V particles was brighter than that of the CS sample and the grain orientation map at IPB was also clearly detected. This indicates that the lattice structure of the CS Ti6Al4V sample at IPB trends to be integrity without defects after HT. The microstructure at the IPB had completely recrystallized into equiaxed nanograins. In particular, the martensitic laths of the deformed region where particle 2 (P2) is synchronously impacted by particle 1 (P1) and particle 3 (P3) is prone to transform into nanograins during HT, while the nanograins at the IPB gradually grow to submicron grains. According to IPF map shown in Fig. 4(f), the lattice distortion caused by adiabatic shear

Fig. 3 Elemental mapping of interfacial microstructure at IPB of cold-sprayed Ti6Al4V deposits using EDS

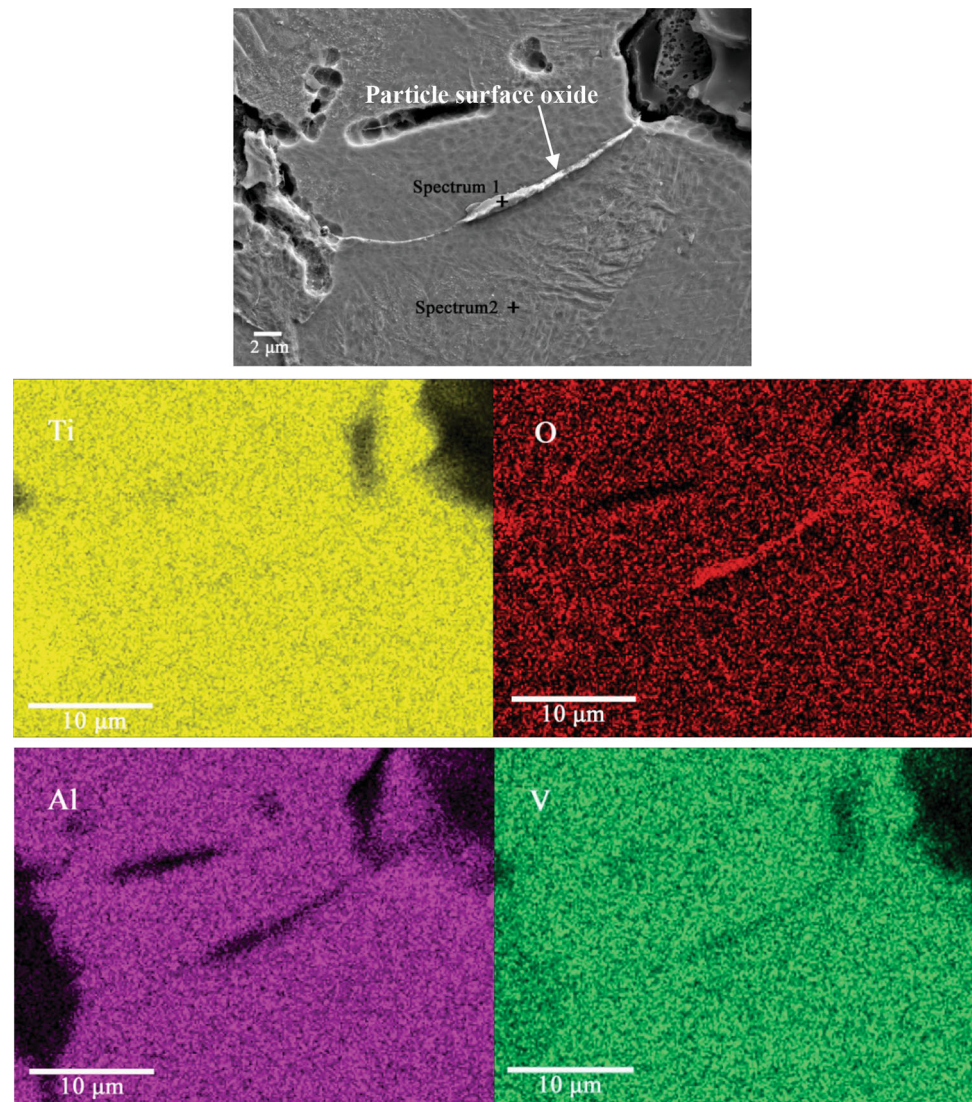


Table 1 Elemental concentrations (wt.%) of the interfacial microstructure at IPB of cold-sprayed Ti6Al4V deposits using EDS

	O	Ti	Al	V
Spectrum1	11.22	87.44	0.80	0.53
Spectrum2	2.76	86.94	6.11	4.19

instability can be significantly eliminated by HT and grain orientation map is completely detected using EBSD (Ref 20). Fig. 4(d) illustrates that the grain size of the HTed sample is larger than that of the CSed sample and the 52.98% of Hex grains size are smaller than 1 μm .

Interfacial Microstructure Characterization by TEM

In order to accurately explore the microstructure characteristics of deformed Ti6Al4V particles in the deposits after HT, the site-specific transmission electron microscope (TEM) lamellae were prepared by focused ion beam (FIB) milling from the particle-particle interfaces to understand the microstructure at this region, as shown in Fig. 5. This FIB technique provides a great advantage over conventional TEM sample preparation by electro-polishing or ion milling as it allows direct imaging of specific locations within the spray-coated sample to provide evidence for the microstructural evolution. The size and thickness of sample cut by FIB are $6 \times 11 \mu\text{m}$ and are about 1 μm , respectively. Then, the sample was thinned to 50 nm by ion milling technique. The sample was characterized by bright field image (BF), dark field image (DF), high-resolution

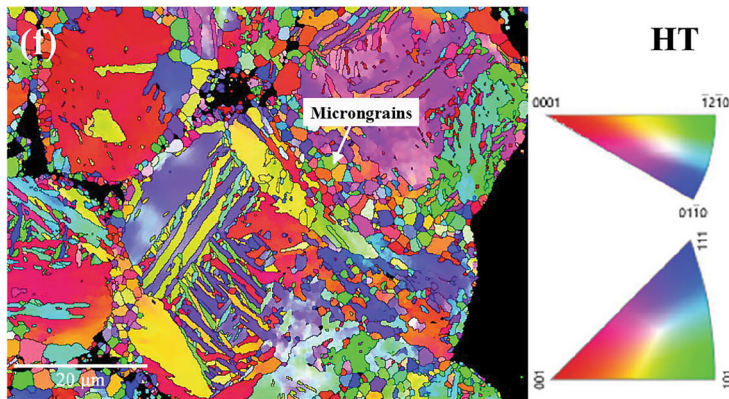
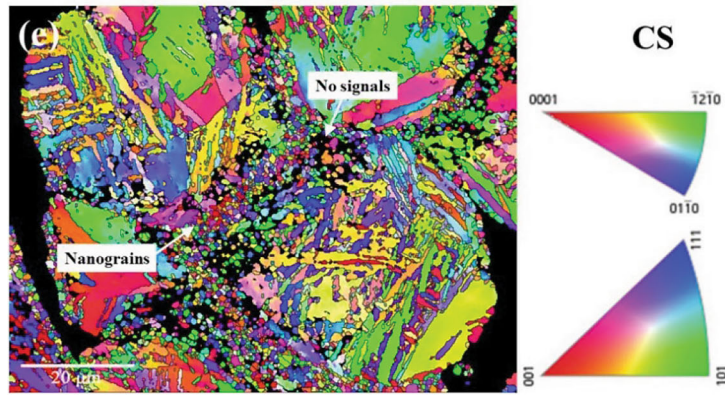
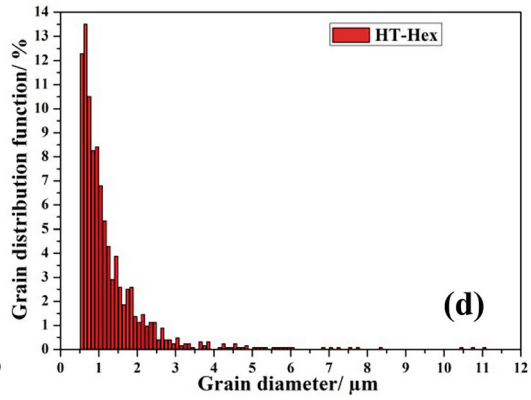
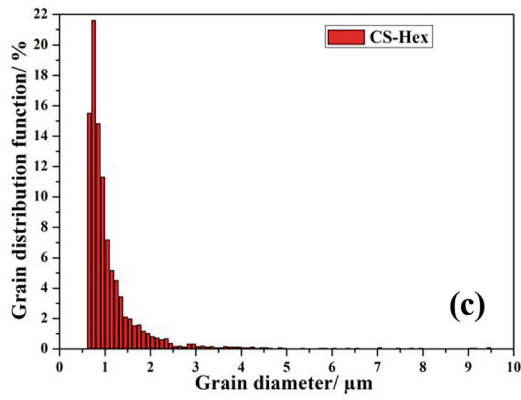
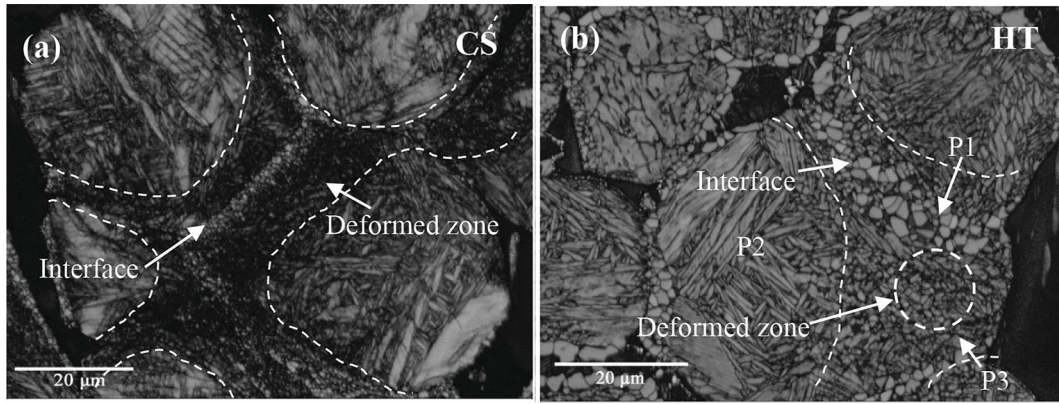


Fig. 4 EBSD images of the cross-sectional microstructure of CS and HT Ti6Al4V deposits: (a) BC map of CS sample, (b) BC map of HT sample, (c) grain distribution of Hex phase in CS sample, (d) grain distribution of Hex phase in HT sample, (e) grain orientation of CS sample, (f) grain orientation of HT sample

transmission electron microscope (HRTEM) and selected area electron diffraction patterns (SADPs).

After HT, the non-uniform evolution of interfacial microstructure of cold-sprayed Ti6Al4V deposits was observed by TEM, as shown in Fig. 6. The BF-TEM images in Fig. 6(a) and (b) give an overview of the microstructure in the vicinity of the interface. The microstructure at IPB is composed of equiaxed grains (Zone 2) near the bonding interface and fine martensitic laths (Zone 1) near the center of particle. There is a distinct boundary between primitive martensitic structure (Zone 1) and deformed nano-equiaxed crystal structure (Zone 2). It is proved that recrystallization of deformed martensite microstructure during Ti6Al4V particles impact is not transferable. The martensite structure in Zone 1 is directional lath, as shown in Fig. 6(c). The diameter of equiaxed grains in Zone 2 is approximately 0.5–1 μm , and the equiaxed grain structure at IPB is perfect, as shown in Fig. 6(d). The high-magnification TEM images and corresponding SADPs at No. 1 and No. 2 are shown in Fig. 6(e) and (f). The clear contrast of the grains and regular feature of the diffraction spots at No. 1 and No. 2 suggests that the crystal defect density has greatly decreased after the HT. The diffraction spots of SADPs at No. 1 and No. 2 present cubic and hexagonal structures, respectively. Fig. 6(e) shows the formation of serrated bulges (white arrow) induced by the dislocations in α grain at the interface between α and β martensitic laths, which leads to the splitting of adjacent β lath (black arrow) into nanograins. From Fig. 6(f), a diffusion layer can be seen at the interface, which indicates the growth of the recrystallized α grains from low dislocation density area to high

dislocation density area. The EDS analysis of equiaxed grains (No. 2) and martensite lath (No.1) structure of HTed Ti6Al4V sample is presented in Table 2. It shows that the Al concentration in No. 2 and the V concentration in No. 1 are 124% and 65% higher than that of No. 1 and No. 2, respectively. The solid solubility of Al element in α -Ti is greater than that in β -Ti, which belongs to α -stabilized elements. V element is a stable element of β -Ti, which has infinite solution in β -Ti. It further proves that the equiaxed grain of No. 2 is α phase, and the martensite lath of No. 1 is β phase.

Grain Boundary Characterization by HRTEM

Further to explore the nano-scale evolution of interfacial nanostructure of HTed Ti6Al4V sample, a high-resolution transmission electron microscope (HRTEM) images were used to observe the martensitic lath boundary, as shown in Fig. 7(a) and (b). In Fig. 7(a), it can be clearly seen that the martensitic lath interface has a significant bulge feature, and the white lath grains are segmented into equiaxed grains by the interfacial bulges. Fig. 7(b) shows the HRTEM of interfacial bulges among the martensitic laths. It can be seen that the interface bulges between two adjacent laths present the characteristics of dislocation tangle in high-resolution state. Fast Fourier transform algorithm (FFT) is performed on the different regions (No. 1, No. 2 and No. 3) of lath grain boundary of in the HRTEM, as illustrated in Fig. 7(c). The FFT-1 lattice structure in No. 1 is cyclized. The FFT-2 lattice structure in No. 2 is hexagonal with deformation characteristics. With the effect of dislocation at grain boundaries, the FFT-3 lattice in No. 3 exhibits a cubic lattice overlap with a certain displacement. The above results suggest that the long lath grains are divided into equiaxed grains under the action of grain boundary bulges induced by dislocation entanglement in the HT process.

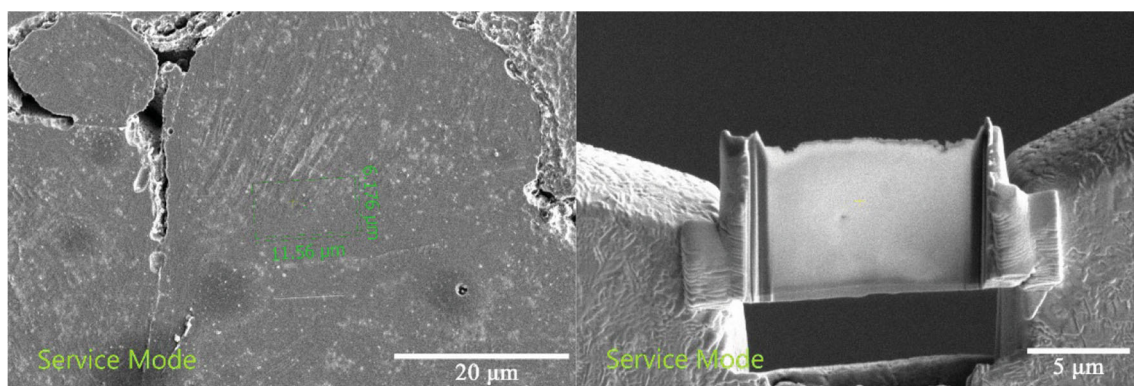


Fig. 5 The location of the extracted lamella (TEM) using FIB between Ti6Al4V particles after HT

Fig. 6 TEM images of the cold-sprayed Ti6Al4V samples at IPB after HT: (a) BF-TEM, (b) magnification of labeled area 1 in (a), (c) martensitic laths, (d) equiaxed grains, (e) SADPs of martensitic laths, (f) SADPs of equiaxed grains

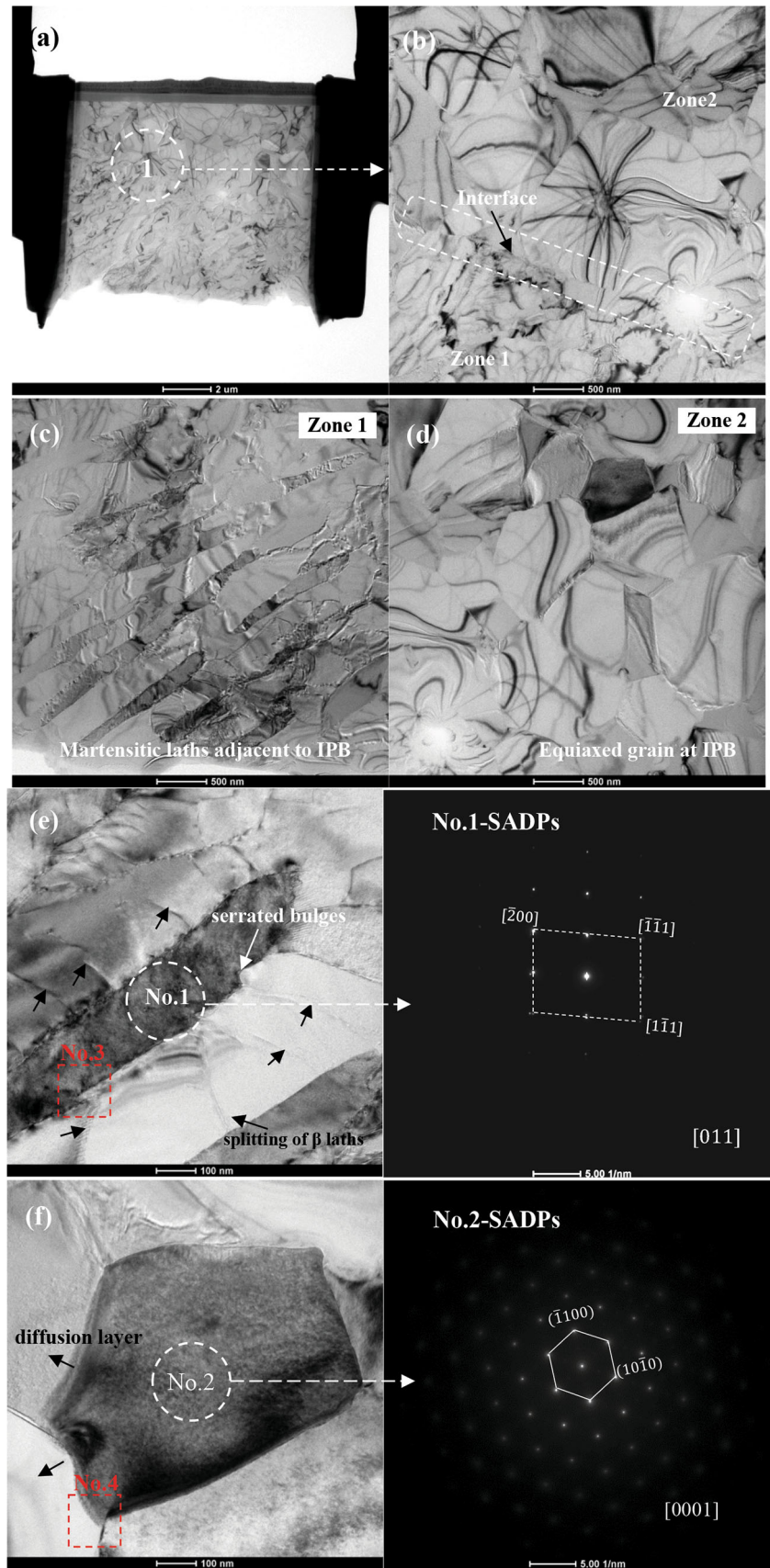
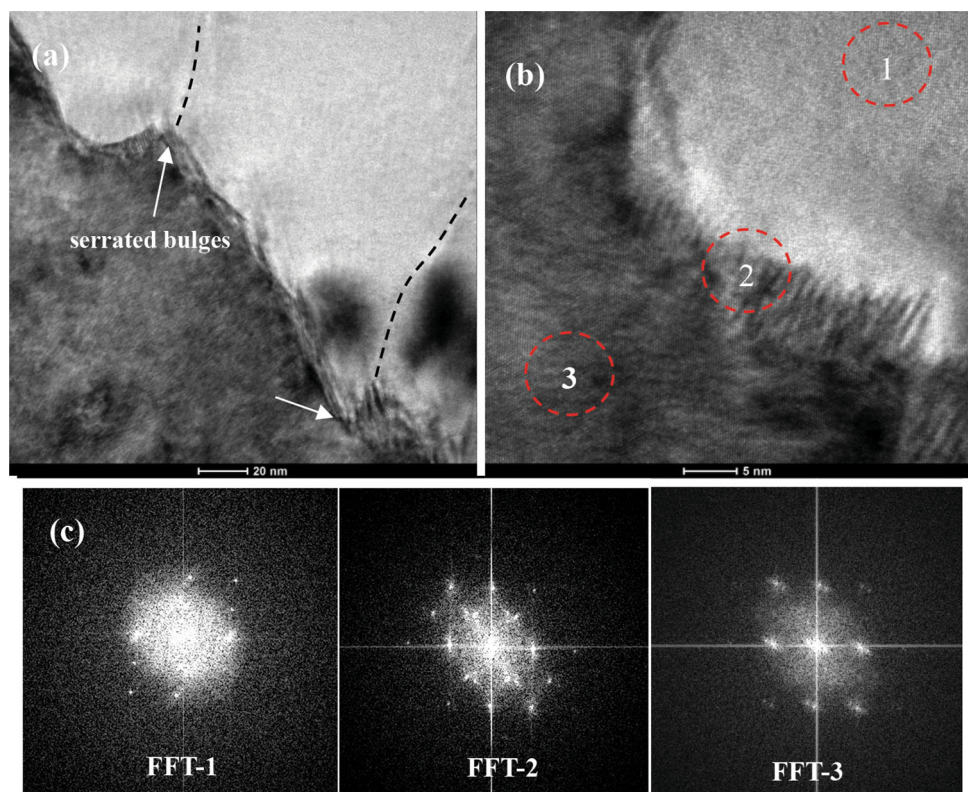


Figure 8(a) and (b) shows the TEM and HRTEM images of equiaxed nanograin boundary. It is obvious that the grain boundary between the black and white nanograins has a transition zone with a thickness of 20 nm. However, there is no transition zone at the interface between white nanograins. FFT images are performed on the different regions (No. 1, No. 2 and No. 3) of equiaxed nanograin boundary in the HRTEM, as illustrated in Fig. 8(c). The corresponding FFT-1 lattice structure in No. 1 region presents continuous diffraction ring. The FFT-2 lattice structure in No. 2 region is hexagonal with deformation characteristics. The FFT-3 lattice in No. 3 region exhibits standard hexagonal diffraction spots. The FFT results demonstrate that during the transformation from martensitic lath to equiaxed grain, the stable grain boundary can be formed only when the high-density dislocation in black grain is gradually eliminated.

Table 2 Elemental concentrations (wt.%) of HTed Ti6Al4V deposits at No. 1 and 2 using EDS

	N	Al	Ti	V
No.1	9.83	2.39	69.87	17.91
No.2	9.22	5.36	74.54	10.88

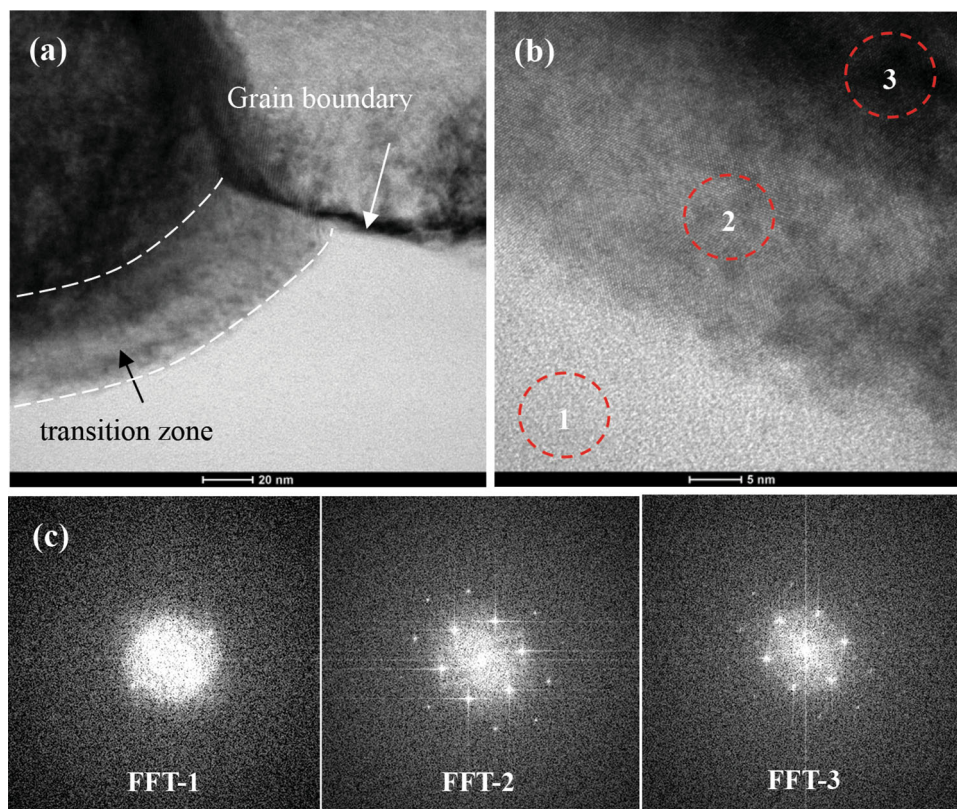
Fig. 7 HRTEM and FFT images at martensitic lath grain boundary of the HTed Ti6Al4V deposits: (a) TEM, (b) HRTEM, (c) FFTs of No.1, 2 and 3 in (b)



Fracture Morphology

According to the SEM and EBSD results in Figs. 2 and 4, the deformed nanocrystalline layer was formed at the IPB of CS Ti6Al4V sample, and there is a clear bonding interface. However, the white oxides and bonding interface at IPB disappear after HT, and the grain size at the IPB is larger than that of the deformed nanograin layer. Fig. 9 shows fracture appearance of CS an HT Ti6Al4V samples. The fracture appearance of CS Ti6Al4V sample has few fracture dimples and most of the Ti6Al4V particles remain in their original deformation states, as shown in Fig. 9(a) - 1 ~ 3. In particular, the surface of Ti6Al4V particles in CS sample has deformation pits with clear boundary, which exhibit no obvious plastic dimples but the plastic flows characteristic after the cracking. Figure 9(b) -1 ~ 3 shows that the fracture morphology of HT samples is completely different from that of CS samples. The fracture appearance of HT Ti6Al4V sample has obvious dimples, which reveals that the HT process promotes the transformation of physical bonding into metallurgical bonding. O element contents in Fig. 9(c) show No.1 ~ 4 at the fracture and surface of CS and HT samples. O contents at fracture (No. 1) and surface (No. 2) of CS Ti6Al4V particle are similar. O content at fracture (No. 3) of HT Ti6Al4V particle is lower than those of CS sample. It can be seen that the deformation nanocrystallization at IPB during CS

Fig. 8 HRTEM and FFT images at equiaxed nanograin boundary of the HTed Ti6Al4V deposits: (a) TEM, (b) HRTEM, (c) FFTs of No.1, 2 and 3 in (b)



impacting cannot cause obvious metallurgical bonding between Ti6Al4V particles.

Nanoindentation Analysis

The samples of nanoindentation test were polished for 6 h using a vibratory polisher with a 0.05 μm colloidal silica attack polish on a medium-napped chemical pad in order to prevent the influence of residual stress on the accuracy of nanoindentation data of Ti6Al4V powder and deposits. Fig. 10(a) and (d) is nanoindentation SEM images of CS and HT samples. The CS sample has obvious particle boundary, while the boundary of HT sample has disappeared. To ensure that the nanoindentation test covers intact Ti6Al4V particles in the deposits, the space between nanoindentations is 3.5 μm . Fig. 10(c) and (d) shows the nanohardness and Young's modulus of Ti6Al4V powder. It can be seen that the Young's modulus at the edge of the Ti6Al4V particle is lower than that at the center. The average nanohardness and Young's modulus of Ti6Al4V powder are 3.87 ± 0.43 and 57.84 ± 11.59 , respectively. Fig. 10(e) and (f) illustrates the nanohardness and Young's modulus of CS and HT Ti6Al4V samples. The dotted line in the curve marks the boundary of the Ti6Al4V particle. The Young's modulus of the particle in the CS sample also shows that the edge is lower than the center. The average nanohardness of CS and HT samples is 4.30 ± 0.52 and

3.95 ± 0.34 , respectively. The nanohardness of CS sample is higher than powder and HT sample due to deformation hardening. The average Young's modulus of CS and HT samples is 90.64 ± 2.33 and $77.82.84 \pm 3.45$, respectively. It is clear that there is no significant variance in average nanohardness of powder, CS and HT samples. However, the average Young's modulus of CS sample is 57% higher than that of the Ti6Al4V powder. After HT, the average Young's modulus was decreased by 16%. It suggests that the increase in Young's modulus at IPB is an important factor affecting the further deformation of Ti6Al4V particles.

Discussion

Combined with the results in Figs. 2 and 4, the martensitic laths of Ti6Al4V particles at IPB are transformed into nanograins by adiabatic shear instability deformation under the high-speed impact of Ti6Al4V particles. There is an obvious boundary and white oxides between the Ti6Al4V particles in the CS sample. It has been proven that the plastic deformation degree of Ti6Al4V particles during the impact is not homogenous in each individual particle and mainly concentrates at the IPB, the combination of severe plastic deformation and high temperature activates the nucleation and grain growth of newly formed equiaxed nanograins and thus boosts the dynamic recrystallization

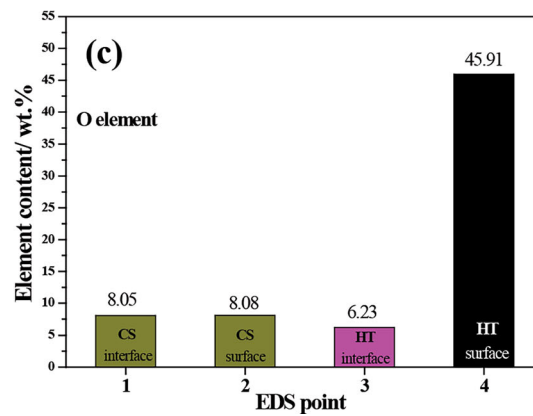
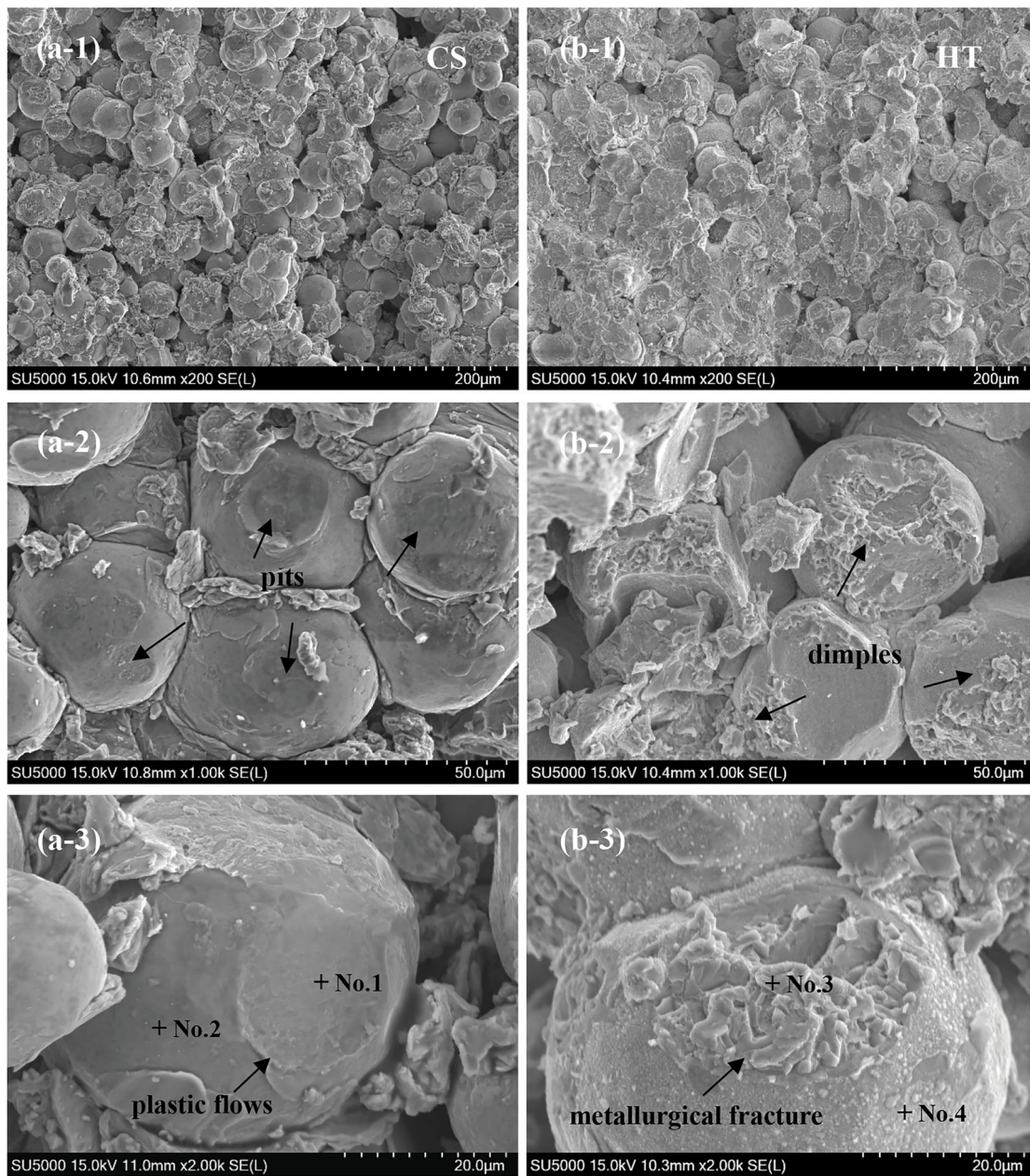


Fig. 9 SEM images of fracture appearance of CS and HT Ti6Al4V samples: (a-1,2,3) CS sample, (b-1,2,3) HT sample, (c) O content of No.1 ~ 4 in Fig. a-3/b-3 using EDS

(Ref 33). In particular, the grain size at the IPB is coarser than that of the deformed layer adjacent to the IPB after HT. The EDS results indicate that there is an oxide layer on the surface of Ti6Al4V powder, and the plastic flow of the Ti6Al4V surface microstructure is caused by the impacting deformation of particles, so that the oxides on the Ti6Al4V surface are squeezed. During particle impact in CS, the cleaning effect by the extrusion of viscous metal jet at the IPB promotes the formation of metallurgical bonding due to the oxides fragments of deformed Cu particle surface (Ref 26). The oxides inclusion among the accumulated Ti6Al4V particles is also an important factor affecting the mechanical properties of CS deposition (Ref 26, 34). The special bonding interface of CS sample can not only disappear through HT, but also make the oxide inclusions at the IPB diffuse into the equiaxed grains.

Since the impact and temperature rise of Ti6Al4V particle at IPB were finished in hundreds of nano-seconds, the recrystallized nanograins transformed from martensitic lath do not have enough time to grow up and finally been observed at the IPB (Ref 9). TEM results show that the dynamically recrystallized nanograins at the IPB have low dislocation density, which are easily to be indexed by EBSD, on the contrary, the deformation nanograin layer adjacent to IPB is difficult to detect the signals using the EBSD due to the accumulation of dislocation and internal stress (See Fig. 4(a)). Therefore, it can be deduced that the dynamic recrystallization of interfacial microstructure has a limited effect on relieving the internal stress in the deformation microstructure of the CS Ti6Al4V particles.

The grain growth at the IPB under HT can play a significant role in the mechanical properties of CS Ti6Al4V deposits. The fracture morphology of the CS deposits indicates that the dynamic recrystallization of the interfacial microstructure is induced by the strong plastic deformation, but it is difficult to form metallurgical bonding between Ti6Al4V particles or the area because of the limited thickness of metallurgical bonding (See Fig. 9). After HT, the bonding boundary between Ti6Al4V particles will completely disappear through HT diffusion. However, it was found that the mechanical properties such as strength and ductility of the HTed CS deposits were usually lower than those of the bulk counterparts (Ref 8, 20, 21, 25). Post-spray HT could also increase the fraction of metallurgical bonding between Ti6Al4V particles at the IPB contributing to the ductility enhancement of the CSed deposit (Ref 31). A significant increase of the interfacial bonding strength was obtained by HT at 950°C

in comparison with as-sprayed Ti6Al4V coating (Ref 21). In brief, the main factors of the poor mechanical properties of cold-sprayed deposits include porosity defects, interfacial oxides, limited interfacial bonding, etc.

The TEM and HRTEM results had also prove that there was an obvious boundary between nanograin and nanomartensite lath in the deformation nanorecrystallization layer. Under adiabatic shear instability deformation of cold spray, the high-density dislocation structures such as dislocation entanglement and dislocation wall are formed in deformed microstructure of Ti6Al4V coating. During the process of dynamic recrystallization, the deformed nanograins transition layer with different dislocation densities and internal stresses is formed. The dislocation density and internal stress of the deformed layer adjacent to the IPB are higher than that of the nanograins structure at IPB. During HT, the nanograins with low dislocation density and internal stress at IPB tend to grow into submicron-equiaxed grains, at the same time, the deformed martensite lath adjacent to the IPB continuously transforms into nanograins. The subgrain boundary formed in the α grain will absorb the dislocation and the orientation difference will continuously increase, so that the original martensite lath were divided into equiaxial ultrafine grains, which is the main reason that the nanograins are formed in the deformation transition region. In summary, the nanograins of the deformed layer in CS grow into submicron-equiaxed grains, on the contrary, the martensitic laths adjacent to IPB exhibits nanograins structure transformation, which indicates that the growth of nanograins at IPB and martensitic laths adjacent to IPB has different growth mechanisms during HT. The growth mechanism of interfacial microstructure of CS Ti6Al4V deposits during HT is shown in Fig. 11. The inhomogeneous growth of the interfacial grains is a new factor causing the poor mechanical properties of the CS Ti6Al4V deposits.

Conclusions

In summary, post-heat treatment is an effective method to improve the mechanical properties of cold spray Ti6Al4V deposits. The interfacial microstructure evolution of the inter-particle boundaries in cold-sprayed Ti6Al4V deposits during the post-heat treatment was studied at the micro- and nano-scale. As a result, the microstructure of original Ti6Al4V powders is coarse martensitic laths. The deformation nanocrystallization at IPB during CS impact cannot cause obvious metallurgical bonding between Ti6Al4V particles. The average Young's modulus of CS Ti6Al4V is 57% higher than that of powder due to high strain rate deformation, but the average Young's modulus of HT sample decreases by 16%. The internal stress and dislocation distribution of interfacial microstructure are uniform

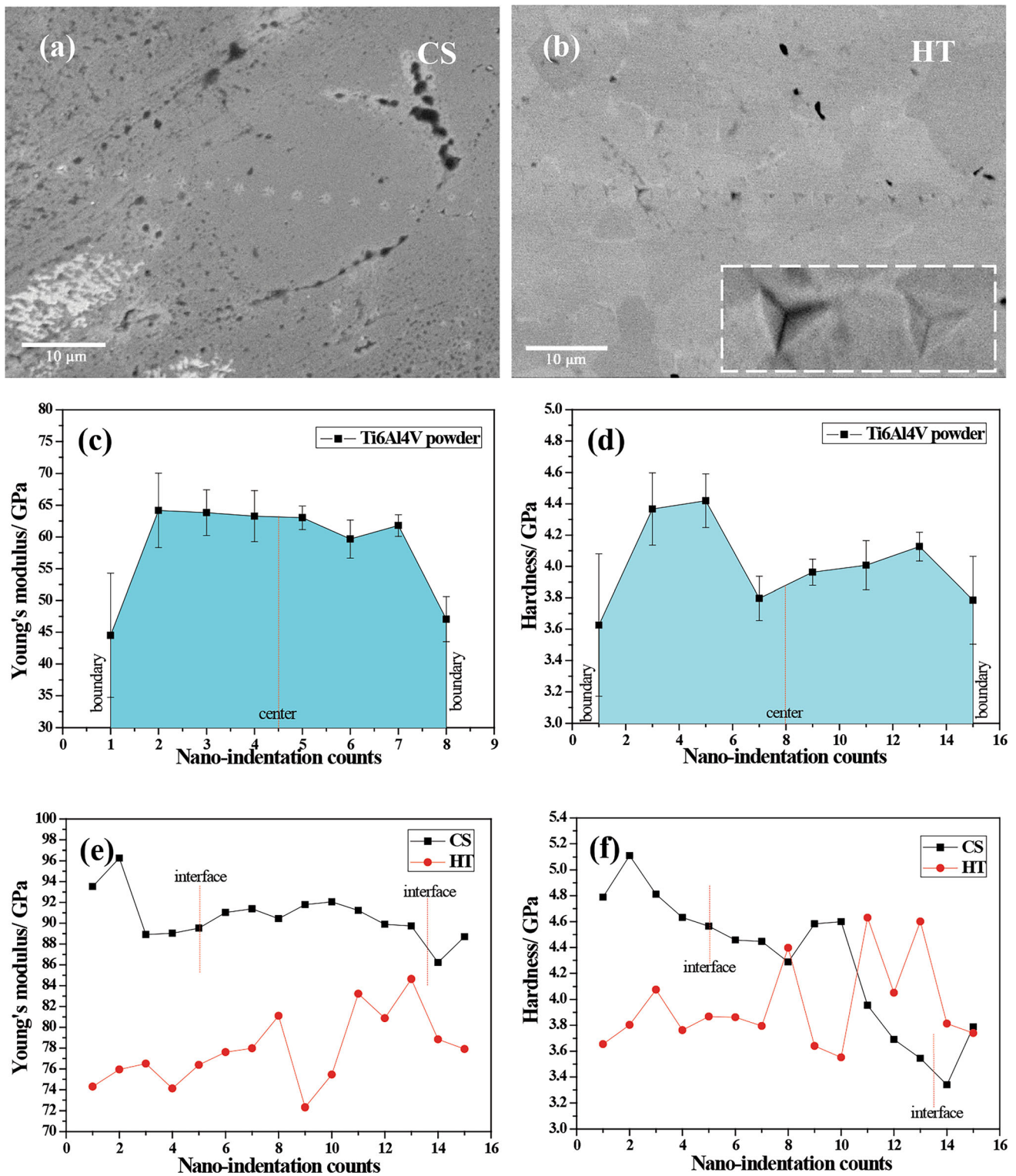


Fig. 10 Nanohardness and Young's modulus in GPa of Ti6Al4V powder, CS and HT samples: (a) nanoindentation SEM of CS sample, (b) nanoindentation SEM of HT sample, (c) Young's modulus of

powder, (d) nanohardness of powder, (e) Young's modulus of CS and HT samples, (f) nanohardness of CS and HT samples

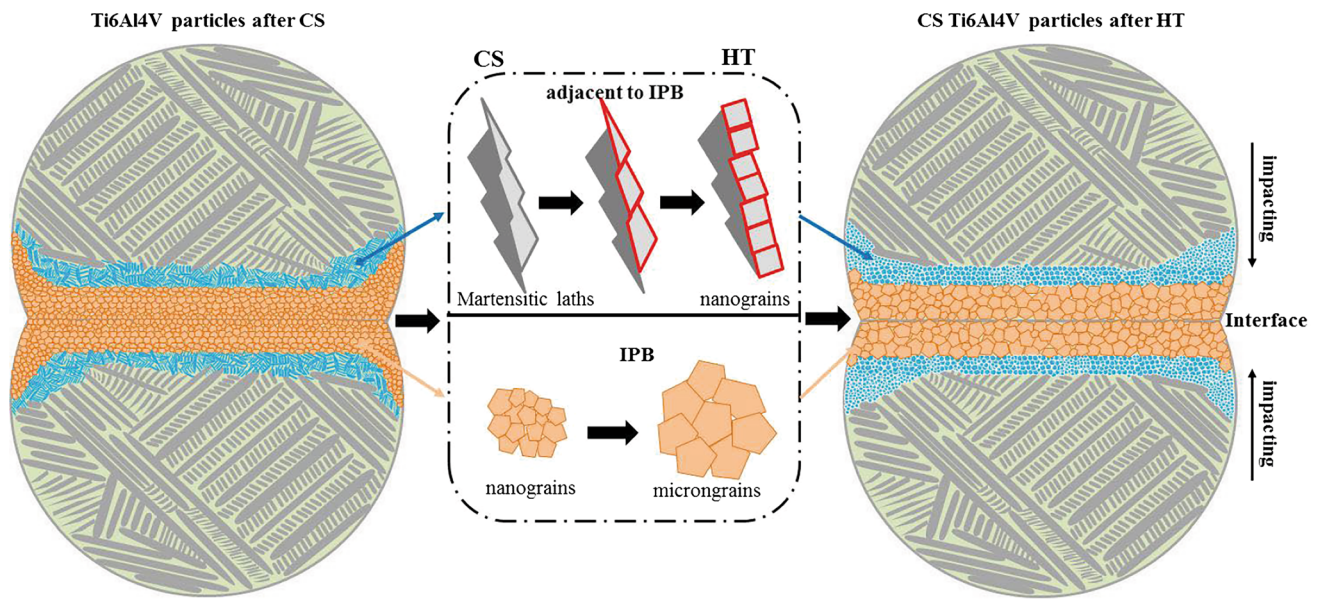


Fig. 11 Evolution of microstructure of deformed Ti6Al4V particles at IPB of CS deposits after HT

due to the different deformation degrees, which results in different growth behaviors and rates of microstructure at deformed layer adjacent to IPB and IPB during HT. The nanograins at the IPB grow into micron-equiaxed grains with the scale of approximately 0.5–1 μm ; on the contrary, the dislocation movement in β grain induces to the formation of serrated bulges at the interface between α and β martensitic laths, which leads to the splitting of adjacent α lath into equiaxed nanograins. The microstructure of deformed particles at the IPB of the CS Ti6Al4V deposits during HT shows non-uniform growth characteristics due to different degrees of deformed microstructure, which reveals the new factor for the poor mechanical properties of CS Ti6Al4V deposits after HT except high porosity and interfacial oxides defects.

Acknowledgments The authors would like to appreciate the financial supports from National Natural Science Foundation of China (51701165) and Natural Science Basic Research Program of Shaanxi Province (2023-JC-YB-318, 2023-JC-QN-0641).

Data Availability Data will be made available on request.

References

- W. Li, C. Cao, and S. Yin, Solid-State Cold Spraying of Ti and Its Alloys: A Literature Review, *Prog. Mater. Sci.*, 2020, **110**, p 100633.
- S. Yin, M. Hassani, Q. Xie, and R. Lupoi, Unravelling the Deposition Mechanism of Brittle Particles in Metal Matrix Composites Fabricated Via Cold Spray Additive Manufacturing, *Scr. Mater.*, 2021, **194**, p 113614.
- Y. Xie, R.-N. Raelison, P. Herve, M.-P. Planche, S. Deng, R. Huang, and J. Wang, Zhongming Ren & Hanlin Liao Strengthened Peening Effect on Metallurgical Bonding Formation in Cold Spray Additive Manufacturing, *J. Therm. Spray Technol.*, 2019, **28**, p 881.
- S. Yin, N. Fan, C. Huang, Y. Xie, C. Zhang, R. Lupoi, and W. Li, Towards High-Strength Cold Spray Additive Manufactured Metals: Methods, Mechanisms, and Properties, *J. Mater. Sci. Technol.*, 2024, **170**, p 47–64.
- D. Guo, M. Kazasidis, A. Hawkins, N. Fan, Z. Leclerc, D. MacDonald, A. Nastic, R. Nikbakht, R. Ortiz-Fernandez, S. Rahmati, M. Razavipour, P. Richer, S. Yin, R. Lupoi, and B. Jodoin, Cold Spray: Over 30 Years of Development Toward a Hot Future, *J. Therm. Spray Technol.*, 2022, **31**, p 2244.
- P. Poza and M.Á. Garrido-Maneiro, Cold-Sprayed Coatings: Microstructure, Mechanical Properties, and Wear Behaviour, *Prog. Mater. Sci.*, 2022, **123**, p 100839.
- A.W.Y.T.N.W. Khun, K.J.W. Bi, and E. Liu, Effects of Working Gas on Wear and Corrosion Resistances of Cold Sprayed Ti-6Al-4V Coatings, *Surf. Coat. Technol.*, 2016, **302**, p 1–12.
- L.I. Perez-Andrade, V.S. Bhattiprolu, W.M. Schuette, and L.N. Brewer, Influence of Powder Properties and Processing Gas on the Microstructural Evolution of Armstrong CP-Titanium and Ti6Al4V Powders Processed by Cold Spray, *Surf. Coat. Technol.*, 2022, **431**, p 128011.
- V.K.C.J.A.M. Birt, R.D. Sisson Jr., and D. Apelian, Microstructural Analysis of Cold-Sprayed Ti-6Al-4V at the Micro- and Nano-Scale, *J. Therm. Spray Technol.*, 2015, **24**, p 1277–1288.
- X.-T. Luo, Y.-K. Wei, Y. Wang, and C.-J. Li, Microstructure and Mechanical Property of Ti and Ti6Al4V Prepared by an In-Situ Shot Peening Assisted Cold Spraying, *Mater. Des.*, 2015, **85**, p 527–533.
- L. Yang, B. Li, J. Yao, and Z. Li, Effects of Diamond Size on the Deposition Characteristic and Tribological Behavior of Diamond/Ni60 Composite Coating Prepared by Supersonic Laser Deposition, *Diam. Relat. Mater.*, 2015, **58**, p 139–148.
- R. Cheng, X. Luo, G. Huang, and C.J. Li, Corrosion and Wear Resistant WC17Co-TC4 Composite Coatings with Fully Dense Microstructure Enabled by In-Situ Forging of the Large-Sized WC17Co Particles in Cold Spray, *J. Mater. Process. Technol.*, 2021, **296**, p 117231.

13. W.J. Feng Guo, G. Tang, Z. Xie, H. Dai, E. Wang, Y. Chen, and L. Liu, Enhancing Anti-wear and Anti-corrosion Performance of Cold Spraying Aluminum Coating by High Current Pulsed Electron Beam Irradiation, *Vacuum*, 2020, **182**, p 109772.
14. Z. Zhao, J. Tang, H. Liu, H. Liu, Y. Ren, M. Tong, L. Yin, H. Du, J. Wang, and T. Xiong, Effect of Rolling Temperature on Microstructure and Mechanical Properties of Ti/Steel Clad Plates Fabricated by Cold Spraying and Hot-Rolling, *Mater. Sci. Eng. A*, 2020, **795**, p 139982.
15. C.J. Huang, X.C. Yan, W.Y. Li, W.B. Wang, C. Verdy, M.P. Planche, H.L. Liao, and G. Montavon, Post-Spray Modification of Cold-Sprayed Ni-Ti Coatings by High-Temperature Vacuum Annealing and Friction Stir Processing, *Appl. Surf. Sci.*, 2018, **451**, p 56-66.
16. P.H. Wen Wang, Y. Wang, T. Zhang, P. Peng, K. Qiao, Z. Wang, Z. Liu, and K. Wang, High-Performance Bulk Pure Al Prepared Through Cold Spray-Friction Stir Processing Composite Additive Manufacturing, *J Mater Res Technol*, 2020, **9**, p 9073-9079.
17. Y. Xu, J. Ge, B. Ji, and W. Li, Mechanical Alloying of Cold-Sprayed Ni-Nb-Si Composite Coating by Friction Stir Processing: Improvement in Microstructure and Resistance Against Molten Silicates Corrosion, *Surf. Coat. Technol.*, 2022, **451**, p 129051.
18. V.S. Bhattiprolu, K.W. Johnson, O.C. Ozdemir, and G.A. Crawford, Influence of Feedstock Powder and Cold Spray Processing Parameters on Microstructure and Mechanical Properties of Ti-6Al-4V Cold Spray Depositions, *Surf. Coat. Technol.*, 2018, **335**, p 1-12.
19. L. Yang, P. Wang, X. Luo, H. Li, H. Yang, S. Wang, and Q. Li, Nanocrystallization of Interfacial Microstructure of Deformed Particles in Cold Sprayed Ti6Al4V Deposits, *Mater. Des.*, 2021, **210**, p 110117.
20. J.Y. Lek, A. Bhowmik, A.W.-Y. Tan, W. Sun, X. Song, W. Zhai, P.J. Buenconsejo, F. Li, E. Liu, Y.M. Lam, and C.B. Boothroyd, Understanding the Microstructural Evolution of Cold Sprayed Ti-6Al-4V Coatings on Ti-6Al-4V Substrates, *Appl. Surf. Sci.*, 2018, **459**, p 492-504.
21. A. Bhowmik, A. Wei-Yee Tan, W. Sun, Z. Wei, I. Marinescu, and E. Liu, On the Heat-Treatment Induced Evolution of Residual Stress and Remarkable Enhancement of Adhesion Strength of Cold Sprayed Ti-6Al-4V Coatings, *Results Mater.*, 2020, **7**, p 100119.
22. M.S. Renzhong Huang, W. Ma, and H. Fukanuma, The Effects of Heat Treatment on the Mechanical Properties of Cold-Sprayed Coatings, *Surf. Coat. Technol.*, 2015, **261**, p 278-288.
23. C.Z.W.-Y. Li, H. Liao, and C. Coddet, Effect of Heat Treatment on Microstructure and Mechanical Properties of Cold Sprayed Ti Coatings with Relatively Large Powder Particles, *J. Coat. Technol. Res.*, 2009, **6**, p 401-406.
24. E.I.P. Vo, J.-G. Legoux, and S. Yue, Mechanical and Microstructural Characterization of Cold-Sprayed Ti-6Al-4V After Heat Treatment, *J. Therm. Spray Technol.*, 2013, **22**, p 954-964.
25. P. Sirvent, M.Á. Garrido, J. Sharp, W.M. Rainforth, and P. Poza, Improving the Oscillating Wear Response of Cold Sprayed Ti-6Al-4V Coatings Through a Heat Treatment, *Surf. Coat. Technol.*, 2020, **399**, p 126128.
26. C. Chen, Y. Xie, R. Huang, S. Deng, Z. Ren, and H. Liao, On the Role of Oxide Film's Cleaning Effect into the Metallurgical Bonding During Cold Spray, *Mater. Lett.*, 2018, **210**, p 199-202.
27. R.T. Yuji Ichikawa, M. Tanno, and K. Ogawa, Elucidation of Cold-Spray Deposition Mechanism by Auger Electron Spectroscopic Evaluation of Bonding Interface Oxide Film, *Acta Mater.*, 2019, **164**, p 39-49.
28. M.D.V. Tian Liu, J.R. Bunn, T. Ungar, and L.N. Brewer, Quantifying Dislocation Density in Al-Cu Coatings Produced by Cold Spray Deposition, *Acta Mater.*, 2020, **193**, p 115-124.
29. H.W. Zhiying Liua, M.J.R. Hache, X. Chu, E. Irissou, and Y. Zou, Prediction of Heterogeneous Microstructural Evolution in Cold Sprayed Copper Coatings Using Local Zener-Hollomon Parameter and Strain, *Acta Mater.*, 2020, **193**, p 191-201.
30. Y. Xie, N. Fan, J. Yang, W. Li, R. Lupoi, X. Guo, R. Huang, and S. Yin, Improvement of Tensile Strength of Cold Sprayed Fe Deposits via in-Process Powder Preheating, *Mater. Lett.*, 2022, **316**, p 132090.
31. J. Tam, B. Yu, W. Li, D. Poirier, J.-G. Legoux, J.D. Giallonardo, J. Howe, and U. Erb, The Effect of Annealing on Trapped Copper Oxides in Particle-Particle Interfaces of Cold-Sprayed Cu Coatings, *Scr. Mater.*, 2022, **208**, p 114333.
32. Y. Cui, Y. Zhao, H. Numata, H. Bian, K. Wako, K. Yamanaka, K. Aoyagi, C. Zhang, and A. Chiba, Effects of Plasma Rotating Electrode Process Parameters on the Particle Size Distribution and Microstructure of Ti-6Al-4 V Alloy Powder, *Powder Technol.*, 2020, **376**, p 363-372.
33. Y. Peng, P. Gao, W. Zhang, L. Cui, S. Liu, W. Chen, J. Li, R. Zhou, G. Liu, Q. Fang, and B. Liu, Severe Plastic Deformation Induced Nano Dispersion and Strengthening Effect in Oxide Dispersion Strengthened Copper Fabricated by Cold Spray Additive Manufacturing, *Mater Charact*, 2023, **205**, p 113281.
34. Y. Xie, S. Yin, C. Chen, M.-P. Planche, H. Liao, and R. Lupoi, New Insights into the Coating/Substrate Interfacial Bonding Mechanism in Cold Spray, *Scr. Mater.*, 2016, **125**, p 1-4.

Publisher's Note Springer Nature remains neutral with regard to jurisdictional claims in published maps and institutional affiliations.

Springer Nature or its licensor (e.g. a society or other partner) holds exclusive rights to this article under a publishing agreement with the author(s) or other rightsholder(s); author self-archiving of the accepted manuscript version of this article is solely governed by the terms of such publishing agreement and applicable law.